

IRAS OBSERVATIONS OF DUST HEATING AND ENERGY BALANCE IN THE RHO OPHIUCHI DARK CLOUD

THOMAS P. GREENE AND ERICK T. YOUNG

Steward Observatory, University of Arizona

Received 1988 April 20; accepted 1988 September 1

ABSTRACT

The total luminosity of the ρ Ophiuchi molecular cloud is derived from *IRAS* data and is found to match the luminosity of known embedded sources very closely. High-resolution 60 and 100 μm band *IRAS* images have been reduced to yield equilibrium color temperature maps and 60 μm band dust optical depth maps for the region. These data, along with optically thin C^{18}O column density data, are used to evaluate dust grain sizes and compositions via competing grain models. Radiative modeling shows that a standard power-law distribution of graphite and silicate grains is responsible for *IRAS* 60 and 100 μm band emissions. These grains are heated to about one-tenth of the cloud's depth in the core region. Their optical depths closely follow molecular column density structure, but these grains are considerably colder than the molecular gas. We also find that a 10 nm minimum particle radius cutoff is appropriate for the 60 and 100 μm band emissions while very small grains or Polycyclic aromatic hydrocarbon molecules dominate the cloud's 12 and 25 μm band emissions.

Subject headings: infrared: sources — interstellar: grains — interstellar: molecules — nebulae: general

1. INTRODUCTION

The ρ Ophiuchi dark cloud is a nearby high-density region undergoing low-mass star formation. *IRAS* maps of the region show much extended emission in all bands on square degree scales as well as many embedded stellar sources. These stars radiatively heat dust grains of various sizes which emit this incident energy in the infrared spectral regime, producing the observed *IRAS* extended emission. Nearly all of the luminosity of the embedded sources is radiated in the infrared by this grain processing. Dust grains must therefore be studied to understand the strength of the cloud's radiation field, its total luminosity, and the geometry of the cloud and its sources. Grain material composition must be determined before the temperatures and optical depths of the dust can be computed. These resultant physical quantities can be compared to molecular gas temperatures and column densities to determine how well the grains and gas are thermodynamically coupled and how deeply into the cloud the grains are heated by the local radiation field.

Models of dust grain sizes and compositions have been largely computed using extinction measurements of thin clouds (e.g., Mathis, Rumpl, and Nordsieck 1977; hereafter MRN). Other models have been constructed to match the far-infrared emission characteristics of thin "cirrus" clouds with no internal energy sources (Rowan-Robinson 1986). The molecular cloud associated with ρ Ophiuchi has much higher column densities than either of these cloud types and may have different grain size distributions and compositions than the thin clouds on which most dust models are based. The ρ Ophiuchi cloud does indeed appear anomalous when compared to the average interstellar cloud; its star HD 147889 has a total-to-selective absorption ratio, $R \approx 4$ (Carrasco, Strom, and Strom 1973; van Breda, Glass, and Whittet 1974; McMillan 1978), whereas the mean R value of galactic interstellar dust is 3.2 (Bohlin and Savage 1981). The ρ Ophiuchi cloud also exhibits a large amount of extended emission in the *IRAS* 12 μm band

(Young, Lada, and Wilking 1986), suggesting a significant mass fraction of very small grains or polycyclic aromatic hydrocarbon (PAH) molecules that are stochastically heated (Sellgren 1984; Léger and Puget 1984). The absorption of starlight by thin interstellar dust clouds can be modeled without the inclusion of such small particles (MRN), and the *IRAS* 60 and 100 μm band emissions can be generally modeled without these particles also (Draine and Anderson 1985). Désert (1986) has developed a model which predicts the flux ratios of *IRAS* bands for an MRN dust model modified to include small grains and PAH molecules illuminated by an interstellar radiation field (ISRF) of 1 to 100 times the solar neighborhood value. We use this model to evaluate the relative contribution of the small grain/PAH component to the *IRAS* data and to determine the minimum size cutoff of the thermodynamic equilibrium emission grain distribution.

The proximity of the ρ Ophiuchi cloud has allowed a detailed study of its dust emission on small scales with *IRAS* data. We study areas as small as a few times 10^{-2} square parsecs and find that regions of this size have more uniform temperatures and optical depths than regions encompassing large fractions of molecular clouds including luminous sources which have been typically used in the construction and evaluation of dust models from FIR observations (Rengarajan 1984; Hildebrand 1983). Only smaller uniform areas can be effectively used in studying radiative energy balance, grain parameters, dust heating depths, and gas-to-dust coupling in detail. The proximity of the ρ Ophiuchi cloud also affords the identification of the dust's principal illuminating sources which must be known in order to evaluate the radiative energy balance of the cloud and the grain materials and size distribution. Many embedded sources have been found in the cloud (Grasdalen *et al.*; Elias 1978; Wilking and Lada 1983; Young *et al.*), but their total number and luminosity is unknown due to their high spatial densities and large obscurations. We now present measurements of the cloud's total luminosity in an effort to determine if undiscovered sources contribute to this value.

II. DATA AND REDUCTIONS

We used two types of *IRAS* data products in our investigation. The SKYFLUX images (*IRAS Explanatory Supplement* 1984) are large-scale ($16^\circ \times 16^\circ$) maps that have been spatially smoothed to $4'$ – $6'$ resolution. These maps have been published in three confirming sets (HCONs) based on time of observation. We used HCON 1 data for our analysis. The HCON 1 observations were chosen for zodiacal emission corrections and 60 and 100 μm band zero-point intensity references since these satellite scans had the most favorable solar elongation angle for minimum zodiacal dust emission.

We used higher resolution images based on all the *IRAS* survey scans of the region for our primary analysis. The full angular resolution of the detector array was realized in these images, hereafter called SURVEY CO-ADD maps, because no spatial smoothing was employed. The approximate area covered by these maps is R.A. = $16^{\text{h}}19^{\text{m}}07^{\text{s}}$ to $16^{\text{h}}28^{\text{m}}57^{\text{s}}$ and decl. = $-25^\circ37'$ to $-23^\circ30'$ (1950). We fitted a linear baseline to the SKYFLUX data in the region of the cloud and subtracted it to remove the zodiacal background emission. The large-scale SKYFLUX images were used to ensure that the emissions being fitted were due to the prevailing zodiacal background and were not due to the cloud itself. An appropriate planar zodiacal baseline model was then subtracted from the SURVEY CO-ADD images to force agreement between the two data sets over approximately 0.25 square degree areas in three corners of the 12 and 25 μm band SURVEY CO-ADD maps. We found that the large-scale background emissions were nearly constant over the 60 and 100 μm SKYFLUX maps, so we subtracted these constant emissions from the respective zero-point corrected SURVEY CO-ADD maps. This set of calibrated and flattened maps was used in all further processing and analysis.

In matching the SURVEY CO-ADD and SKYFLUX intensity levels, a number of instrumental effects had to be accounted for. Individual satellite scan paths are clearly visible as “stripes” on both the SURVEY CO-ADD and SKYFLUX images. These stripes are produced by differences in detector gains between scans and by scan-to-scan differences in the baselines. In a second effect, the reponse of the detectors to infrared radiation temporarily increases after passing over a bright source. These problems dictated that the areas chosen for intensity matching be large enough to contain many scan stripes to average the variable gain effects and also be in an area unaffected by detector hysteresis problems. We chose such a box defined by R.A. = $16^{\text{h}}25^{\text{m}}57^{\text{s}}$ to $16^{\text{h}}28^{\text{m}}57^{\text{s}}$ and decl. = $-25^\circ37'10''$ to $-24^\circ53'27''$ (1950) for matching intensities between the 60 and 100 μm SURVEY CO-ADD and SKYFLUX plate 159 maps. The 0.25 deg² regions used in flattening the 12 and 25 μm maps also contain several satellite scans and well removed from bright sources.

Millimeter wave data were taken from Wilking and Lada (1983; hereafter WL). We used their optically thin C^{18}O map and resultant LTE column densities of the cloud core region in conjunction with the reduced set of *IRAS* maps.

III. ANALYSIS AND RESULTS

The set of reduced images was processed to yield temperature and optical depth maps of emission from dust grains in LTE. We assumed that 60 and 100 μm band images resulted from such emission while the 12 and 25 micron band intensities may be dominated by stochastic radiation processes. Equi-

librium emission grain temperature maps were created for the central cloud region by integrating diluted blackbody emission weighted by the relative *IRAS* system response $R(\lambda)$ over the *IRAS* 60 and 100 μm bandpasses. We evaluated the expression

$$\frac{\int_{\lambda 60} B_{\lambda}(T)\lambda^E R(\lambda)d\lambda}{\int_{\lambda 100} B_{\lambda}(T)\lambda^E R(\lambda)d\lambda} \quad (1)$$

for a distribution of temperatures T spaced by 0.5 K and piecewise fit polynomials to the temperatures as a function of these ratios. Grain temperatures were determined by evaluating these polynomial functions for 60 to 100 μm band flux ratios in each pixel of the reduced data set. The resultant T values are emission-weighted temperatures in each column. Emissivities $\epsilon \propto \lambda^{-1}$ and $\epsilon \propto \lambda^{-2}$ ($E = -1, -2$) were used to calculate two dust temperature maps for this region.

We assumed the cloud to be optically thin over the 60 μm band so optical depths were calculated from

$$\tau_{60} = \frac{I_{60}}{\int_{\lambda 60} B_{\lambda}(T)R(\lambda)d\lambda} \quad (2)$$

for the in-band intensity I_{60} and temperature T at each pixel. The most opaque region of the cloud was found to have an optical depth of less than 0.1 so this optically thin approximation appears valid. Two optical depth maps were also generated: one for each emissivity function and its corresponding temperature distribution. In Figure 1 ^{12}CO temperature contours overlay the $\epsilon \propto \lambda^{-2}$ dust temperature map, but careful consideration is required before these two temperature maps are compared. The ^{12}CO temperature contours are taken from Loren *et al.* (1980) and represent peak ^{12}CO temperatures at each location. The isotope ^{12}CO is heavily self-absorbed throughout the cloud core and also shows self-absorption in much of the cloud periphery (Lada and Wilking 1980) so a peak temperature value is necessarily between the hotter interior and cooler exterior temperatures of a self-absorbed line. The isotope ^{12}CO also becomes optically thick quickly with distance into the cloud so the ^{12}CO temperatures sample only the outer cloud “skin” where $\tau(^{12}\text{CO}) < 2-4$. Our dust temperatures, however, sample a deeper column of the cloud whose depth is determined later in this paper. We interpret the dust to be isothermal in each column from the surface to a depth beyond which the grains have temperature too low to substantially contribute to the luminosity of the column. In reality each column must have a distribution of temperatures with grains in the most intense radiation field being hottest. Dust temperatures appear to be nearly high enough in and near the cloud core to be heating the gas to the temperatures in Figure 1, but in reality the deeper parts of the cloud have higher gas temperatures (35 K, Wilking 1981) and lower dust temperatures. *The CO must therefore be heated by a source of energy other than grain collisions in the bulk of the cloud.*

The $\tau \propto \lambda^{-2}$ optical depth map of Figure 2 with $N_{\text{C}^{18}\text{O}}$ contours (WL) also requires a somewhat complicated interpretation. Equation (2) computes optical depths for the fraction of a column of dust which is heated to temperature T . We later argue that this fraction is a function of illumination geometry and is small compared with the gas column depth. The optical depths computed from equation (2) must be lower limits since grains considerably colder than the emission-averaged temperature T do not contribute to these determined temperature and optical depth values. Uniform grain illumination will

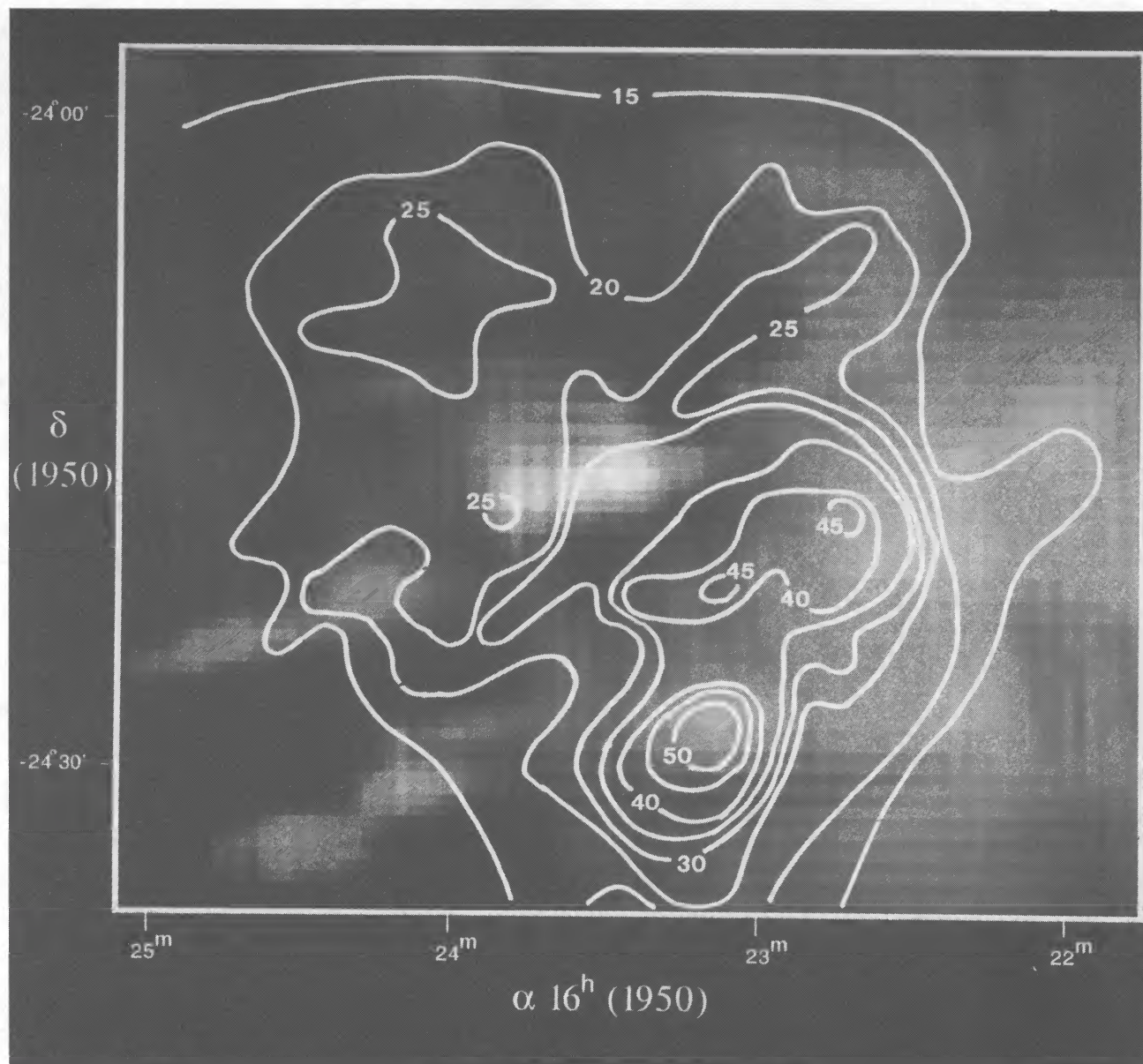


FIG. 1.—Linear gray scale dust temperature map from 60 and 100 μm band *IRAS* data assuming $\epsilon \propto \lambda^{-2}$ emissivity law. Grain temperatures range from 18 K to 40 K. ^{12}CO temperature contours (K) are from Loren *et al.* (1980).

nevertheless produce an optical depth map which is morphologically similar to an optically thin molecular column density map and this is observed in Figure 2. Detailed departures between τ_{60} and $N_{\text{C}^{18}\text{O}}$ structures must be examined carefully, however. Embedded cloud sources warm up nearby dust more than the cloud's general radiation field, producing elevated temperatures near these sources in Figure 1. Equation (2) calculates optical depths of this locally heated material which are necessarily small for all low-luminosity sources, so Figure 2 shows departures from C^{18}O contours near embedded sources which cause local heating seen in Figure 1. The agreement between τ_{60} and $N_{\text{C}^{18}\text{O}}$ becomes better on smaller scales once this is considered. We also note that the τ_{60} maximum of Figure 2 coincides with the dense core ρ Oph A (Loren *et al.* 1980), but there is no τ_{60} or $N_{\text{C}^{18}\text{O}}$ peak at the location of the ρ Oph B core (Loren *et al.* 1980).

a) Energy Balance

We divided a box from R.A. = $16^{\text{h}}20^{\text{m}}00^{\text{s}}$ to $16^{\text{h}}26^{\text{m}}00^{\text{s}}$ and decl. = $-25^{\circ}00'00''$ to $-23^{\circ}30'00''$ (1950) into nine regions, each of size $2^{\text{m}}\text{R.A.} \times 30' \text{ decl.}$ (see Fig. 3). The integrated flux was computed for each *IRAS* band by multiplying the mean intensity value ($\text{W m}^{-2} \text{sr}^{-1}$) of each region by the solid angle subtended by that region. We also calculated mean equilibrium grain temperatures and 100 μm optical depths of each region from maps produced by equation (1) and equation (2) modified for the *IRAS* 100 μm band parameters. The flux of the ρ Oph cloud between 8 and 42.5 μm was approximated by summing the *IRAS* 12 and 25 μm band fluxes, and linearly interpolating between these bands and the 60 μm band. We used the FIR (Lonsdale *et al.* 1985) parameter to estimate the flux between 42.5 and 122.5 μm with *IRAS* 60 and 100 μm

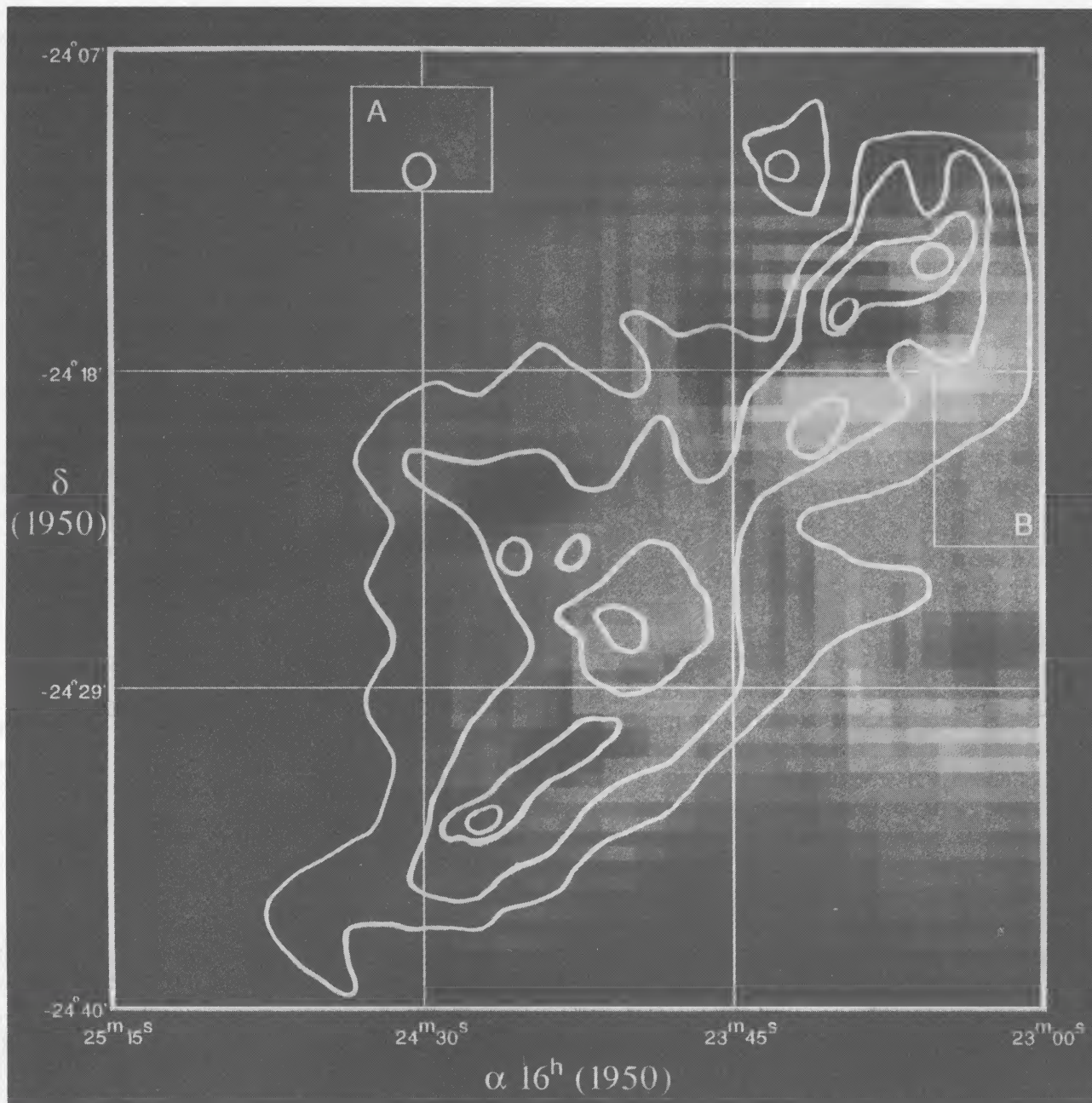


FIG. 2.—Linear gray scale $60\ \mu\text{m}$ optical depth map assuming $\epsilon \propto \lambda^{-2}$ grain emissivity. Optical depths range from 3.0×10^{-3} to 7.6×10^{-2} . N_{ClSO} column density contours (10^{16} to $2.5 \times 10^{16}\ \text{cm}^{-2}$) are from Wilking and Lada (1983).

band fluxes, and we numerically integrated the optically thin flux of a dilute blackbody beyond $122.5\ \mu\text{m}$. The numerical integration was done for the mean $60/100$ grain temperature, $T_{60/100}$, and $100\ \mu\text{m}$ optical depth, τ_{100} , for each region:

$$F(122.5\ \mu\text{m} - 3\ \text{mm}) = \int_{122.5\ \mu\text{m}}^{3\ \text{mm}} B_{\lambda}(T_{60/100})\tau_{100} * \left(\frac{\lambda}{100\ \mu\text{m}}\right)^E d\lambda. \quad (3)$$

This far-infrared–submillimeter flux integral was done for emissivities proportional to λ^{-1} and λ^{-2} ($E = -1, -2$), the two values used in the studied interstellar dust models. To estimate the flux from the cloud at wavelengths below the

IRAS short-wavelength limit, we used *IUE* (Bohlin and Savage 1981), *BV* (SAO), *RI* (Chini 1981), and *JHKL* (Harris, Woolf, and Rieke 1978) photometry for HD 147889, the most luminous source in the cloud. This is clearly a lower limit to the cloud's flux in these bandpasses because some light is scattered away from HD 147889 by the cloud's intervening dust. Fluxes in each spectral region were converted to luminosities assuming a distance of 160 pc (Whittet 1974). Results are presented in Table 1.

The Kramers-Kronig dispersion relation (Purcell 1969) also forces the emissivity to steepen from $\epsilon \propto \lambda^{-1}$ at long wavelengths (Rowan-Robinson 1986). The $120\ \mu\text{m}$ to $3\ \text{mm}$ luminosity in the $\epsilon \propto \lambda^{-1}$ case is therefore an upper limit. A $\lambda = 250$

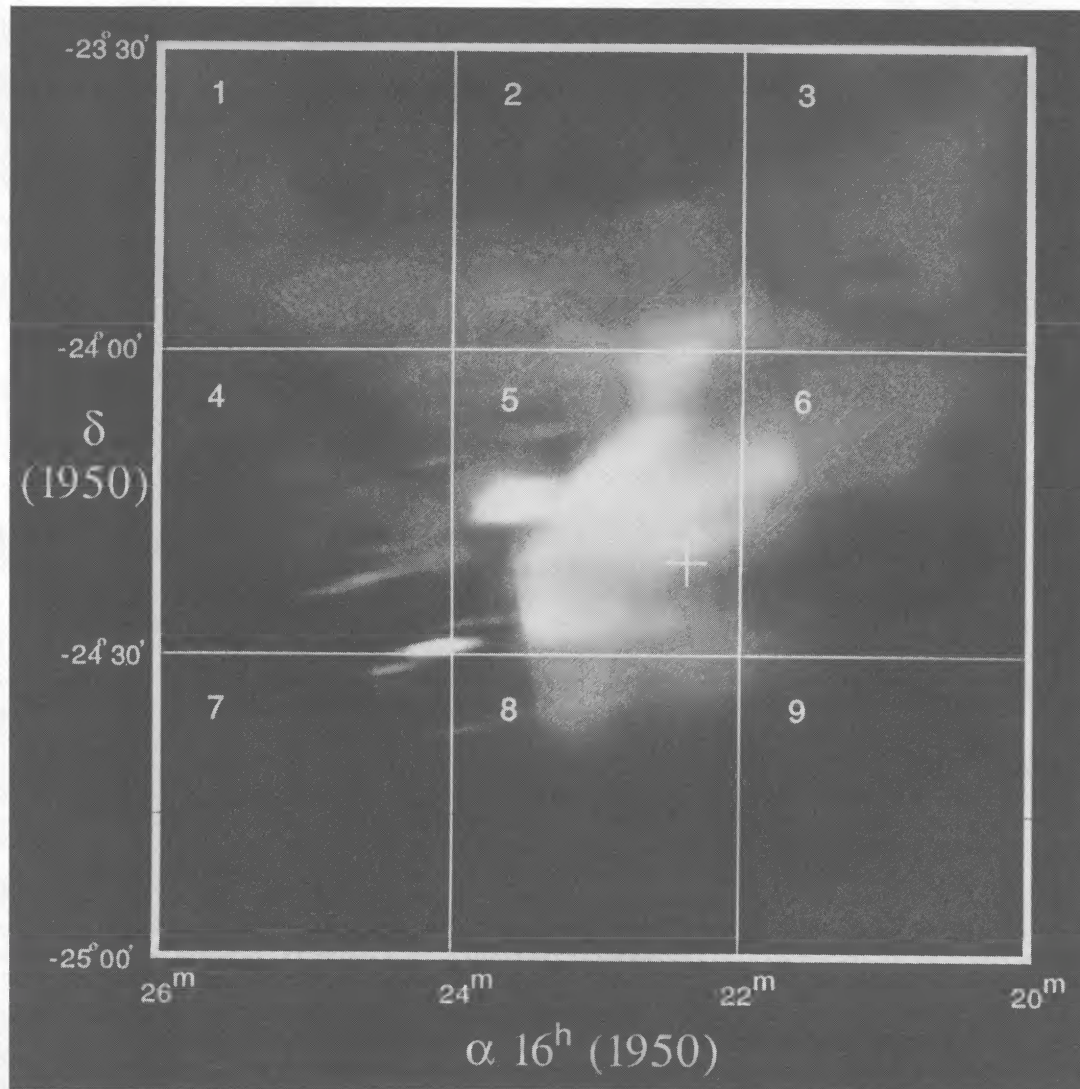


FIG. 3.—Linear gray scale $12\ \mu\text{m}$ band intensity map of the ρ Ophiuchi dark cloud with global regions 1–9 used in energy balance analysis outlined. The position of HD 147889 is marked with a cross.

μm turnover suggested by Hildebrand (1983) would lower this quantity by approximately only $90 L_{\odot}$ so its effect on the total cloud luminosity is minor. The total luminosity of known sources in the cloud is $6700 L_{\odot}$ (WL; Lada and Wilking 1984). The Sco OB2 association also contributes approximately 1000

TABLE 1
LUMINOSITIES (L/L_{\odot}) FOR $\epsilon \propto \lambda^{-1}$, $\epsilon \propto \lambda^{-2}$ EMISSIVITIES

Wave Band (μm)	$\epsilon \propto \lambda^{-1}$	$\epsilon \propto \lambda^{-2}$	Comments
0–8	37.2	37.2	HD 147889 data
8–15	979	979	IRAS $12\ \mu\text{m}$ band
15–18	244	244	Interpolation
18–30	276	276	IRAS $25\ \mu\text{m}$ band
30–42.5	387	387	Interpolation
42.5–122.5	3557	3557	FIR = $1.26[F(60) + F(100)]$
120–3000	2360	1560	Dilute BB integration
Total	7840	7040	Probably a lower limit: photometry below $8\ \mu\text{m}$ done with small aperture

L_{\odot} to the cloud by irradiating the cloud's surface (approximately $10\ \text{pc}^2$) with an absorbed flux of $5 \times 10^{-2}\ \text{ergs s}^{-1}\ \text{cm}^{-2}$ (Ryter Puget, and Perault 1987). This combined known input luminosity ($7700 L_{\odot}$ and $7040 L_{\odot}$ for $\epsilon \propto \lambda^{-1}$ and $\epsilon \propto \lambda^{-2}$, respectively). This suggests that either emissivity may be appropriate and contributions to the cloud luminosity from unknown external or hidden internal sources must be minimal. The observed luminosity of the cloud is dominated by the three known B stars HD 147889, S1, and SR 3 as well as the Sco OB2 radiation field. The rough agreement of emitted luminosity with known luminosity sources also refutes the existence of a population of low-luminosity sources which cannot be detected individually but collectively contribute substantially to the cloud's luminosity.

b) Dust Analysis

i) Region Analyzed

We selected a central region of the cloud for analysis with the criteria of high dust and gas optical depths and the availability of optically thin molecular line column density data.

This region is close to the exciting B stars in the western segment of the cloud and coincides with maximum molecular density. Figure 2 shows the 45° R.A. \times $11'$ decl. areas used in our grain size analysis as well as the two regions A and B we studied in detail in our dust composition analysis. This grain material investigation required knowledge of dust optical depths and gas column densities so it was limited to regions covered by the WL $N_{C^{18}O}$ map. Only regions A and B are both covered in the $C^{18}O$ map and contain no discrete embedded IRAS sources which would differentially heat material and would not be representative of the grains producing the cloud's diffuse emission. Both regions are less than 5×10^{-2} pc² projected area, and we determined their freedom from sources by visual analysis of the reduced IRAS maps. Although the ^{13}CO data of Encrenaz, Falgarone, and Lucas (1975) covers regions farther from the cloud core, this emission is optically thick over its extent and therefore not useful for calculating column densities.

ii) Dust Size Analysis

A dust size distribution was determined by comparing 12/25 μ m versus 60/100 μ m flux density ratios for different regions in the cloud core by plotting each pixel in these regions and comparing the plots to the Désert (1986) model of IRAS emission. This model consists of PAH molecules emitting in spectral bands and an MRN type distribution of graphite and crystalline silicate grains in thermal equilibrium between sizes a_{\min} and a_{\max} such that the number of grains, n , is given by

$$dn \propto a^{-3.5} da. \quad (4)$$

The entire SURVEY CO-ADD map, the $2'' \times 30'$ regions used in the energy balance determination, and each core region are plotted in Désert's color-color diagram in Figure 4.

Desert's model, indicated by a dashed line in Figure 4, suggests that the dust in the core region as well as the cloud as a whole is consistent with an MRN distribution with a small size cutoff $a_{\min} = 10$ nm supplemented by a population of PAH molecules. Core regions free of embedded sources have the most uniform radiation field and also fall closest to Désert's $a_{\min} = 10$ nm model curve. The model's decrease in $F_{\nu}(12)/F_{\nu}(25)$ with increasing radiation field (x) is a result of thermal emission increasing in the 25 μ m band. The Ophiuchus regions with embedded sources have smaller $F_{\nu}(12)/F_{\nu}(25)$ than predicted by the model for $F_{\nu}(60)/F_{\nu}(100) \geq 0.3$. We suggest that this is due to photodissociation of PAH molecules in the radiation fields surrounding young stellar objects which would decrease grain emissions in the 12 μ m band, while the longer wavelength fluxes would increase due to the higher equilibrium temperatures of the large grain population. Young *et al.* suggested the general abundance of very small grains in the Ophiuchus cloud upon examination of the extended emission in the 12 μ m band IRAS image, and Vrba *et al.* (1975) suggested that the mean size of the grains responsible for the absorption (and therefore emission) was abnormally large because of the high total-to-selective absorption ratio toward S1, a B star embedded in the cloud. Our observations of a large very small grain/PAH population and a large mean size of equilibrium emitting grains is therefore consistent with these earlier observations.

Figure 4 also indicates that the incident radiation field in the infrared emitting region is between about 5 and 50 times the solar neighborhood ISRF value. Figure 5 shows the entire SURVEY CO-ADD region plotted along with the data presented by Désert (1986). Désert's data points are from 30' averaged beams of galactic molecular areas, about the size of the ρ Ophiuchi cloud if it were at 1 kpc. This figure allows a comparison of the ρ Ophiuchi cloud with other molecular clouds in

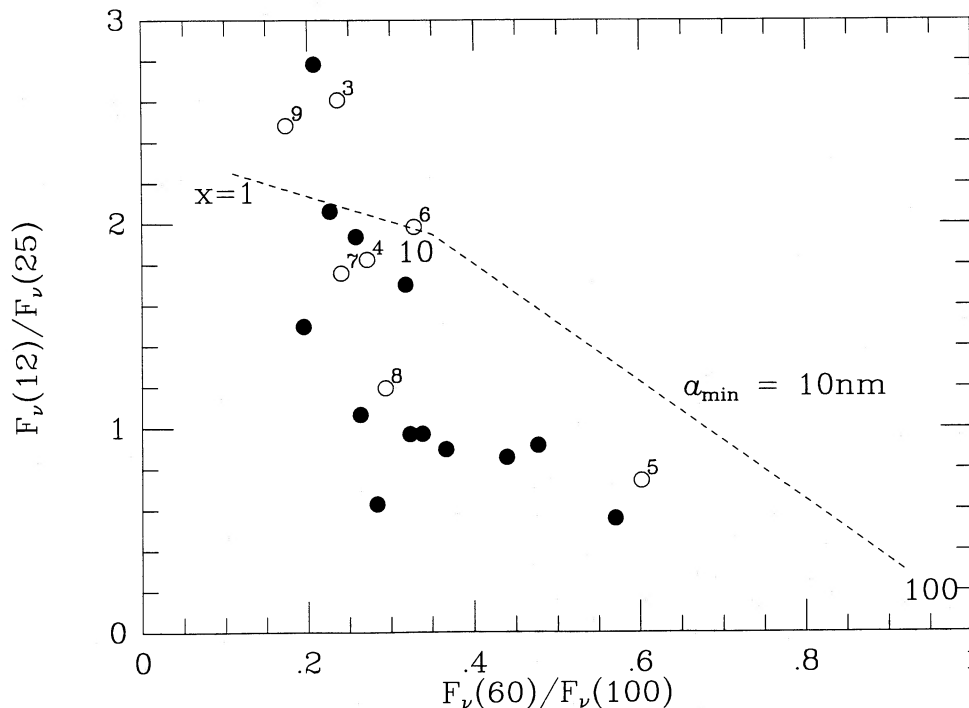


FIG. 4.—Color-color plot of dust emission. Line is from model of Désert (1986). $x = 1$ denotes solar neighborhood radiation field, while $x = 100$ denotes 100 times enhancement. Filled circles are IRAS data for the core region (Fig. 2); open circles are numbered for global regions 3–9 (Fig. 3; see text).

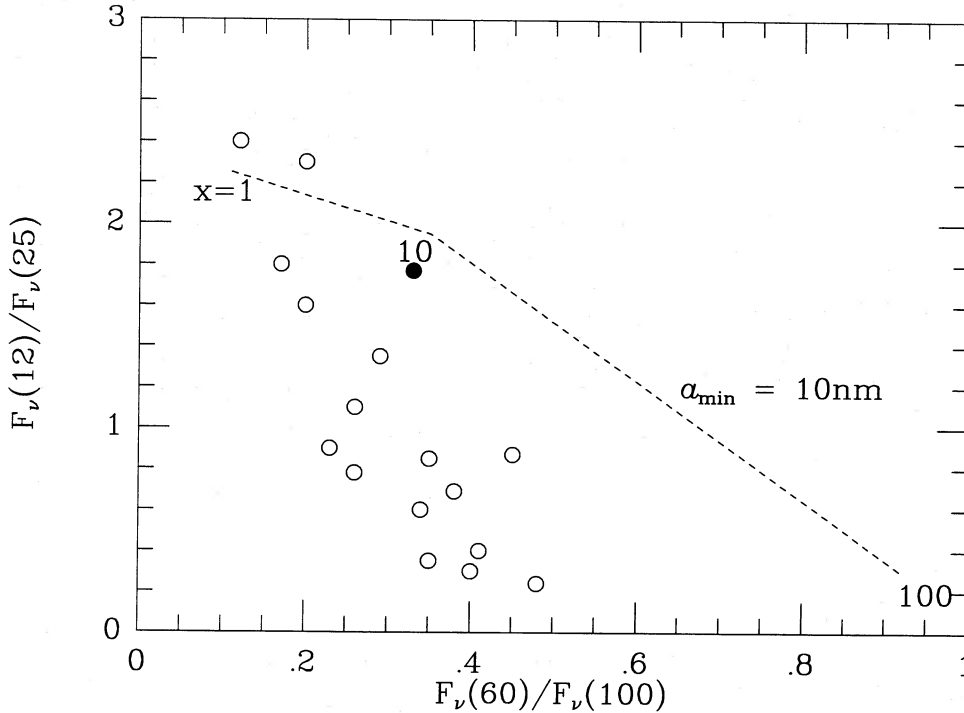


FIG. 5.—Color-color plot of *IRAS* data for emission from entire SURVEY CO-ADD region (filled circle) plotted with galactic plane regions (open circles) of similar projected area from Désert (1986).

the Galaxy and shows that other molecular clouds are similar to subregions within the ρ Ophiuchi cloud. The ρ Ophiuchi regions (Fig. 4) are distinguished by somewhat higher $F_{\nu}(12)/F_{\nu}(25)$ for a given $F_{\nu}(60)/F_{\nu}(100)$ than the molecular regions plotted in Figure 5. $F_{\nu}(12)/F_{\nu}(25)$ of the entire cloud is also higher than that of any other molecular regions with the same radiation field in Figure 5. This suggests a larger population of PAHs in the ρ Ophiuchi cloud than other molecular regions.

iii) Dust Composition Analysis

We now determine dust grain material composition via modeling of grain emission and analyze consequential heating depths into the cloud. Our primary goal is determining whether the cloud's grains are amorphous carbon and silicates with mid-infrared emissivities $\epsilon \propto \lambda^{-1}$ or graphite and crystalline silicates with mid-infrared emissivities $\epsilon \propto \lambda^{-2}$. We have used only 60 and 100 μm band data in analyzing the dust heating depths since the stochastic emission processes responsible for 12 and 25 μm band emission are not understood well enough to yield grain composition information from these bands. The 12 μm emission (Fig. 3) is particularly extended and consists of a very thin layer of emission which is not correlated well with the 60 μm or C^{18}O optical depths. We find the ratios of 12 to 25 and 25 to 60 μm in-band fluxes to be flat over a large range of 60 to 100 in-band flux ratios. This behavior is inconsistent with thermal equilibrium emission in the 12 and 25 μm bands. Figure 6 shows that the 25 to 60 μm in-band *IRAS* flux ratios do not follow the theoretical curves for the either amorphous or crystalline grains in thermal equilibrium. The points plotted in Figure 6 are from a high ambient radiation field area between region *B* (Fig. 2) and HD 147889.

The crystalline grain model by MRN with Draine and Lee (1984; hereafter DL) emissivities and abundances and the mostly amorphous model proposed by Rowan-Robinson (1986) are evaluated by comparing their predicted fluxes in the cloud's known radiation field to *IRAS* observations. Both models are composed of carbon and silicate materials. We evaluate equation (4) from 10 nm to 300 nm to determine a mean grain size of 30 nm for the crystalline model and adopt the emissivities and abundances computed for this size by DL. Over 90% of the Rowan-Robinson model's emission arises from an $\epsilon \propto \lambda^{-1}$ component with a 100 nm grain size (the remainder is $\epsilon \propto \lambda^{-2}$) in the 60 and 100 μm *IRAS* bands. We therefore use Rowan-Robinson's published (1986) emissivities for these grains with an emissivity turnover to $\epsilon \propto \lambda^{-2}$ at $\lambda = 250 \mu\text{m}$ wavelength as discussed in our energy balance analysis.

We interpret the radiation field in the cloud core with a simplified cloud model and the ratios of 60 and 100 μm band *IRAS* fluxes. HD 147889, S1, and the Sco OB2 association are the heating sources. The stars are assumed to be embedded in the cloud which is represented as a slab of uniform density, and flux from the Sco OB2 association is incident on the face of the slab. Flux absorbed from these sources by each grain component *i* of each model at any point in the slab is

$$F_i = \iint B_{\lambda}(T_{\text{HD}}) Q_i(\lambda) t(\lambda) d\lambda d\Omega + \iint B_{\lambda}(T_{\text{S1}}) Q_i(\lambda) t'(\lambda) d\lambda d\Omega + \int F_{\lambda, \text{Sco}} Q_i(\lambda) t''(\lambda) d\lambda, \quad (5)$$

where $T_{\text{HD}} = 2.2 \times 10^4 \text{ K}$, $T_{\text{S1}} = 1.75 \times 10^4 \text{ K}$, $Q_i(\lambda)$ is the

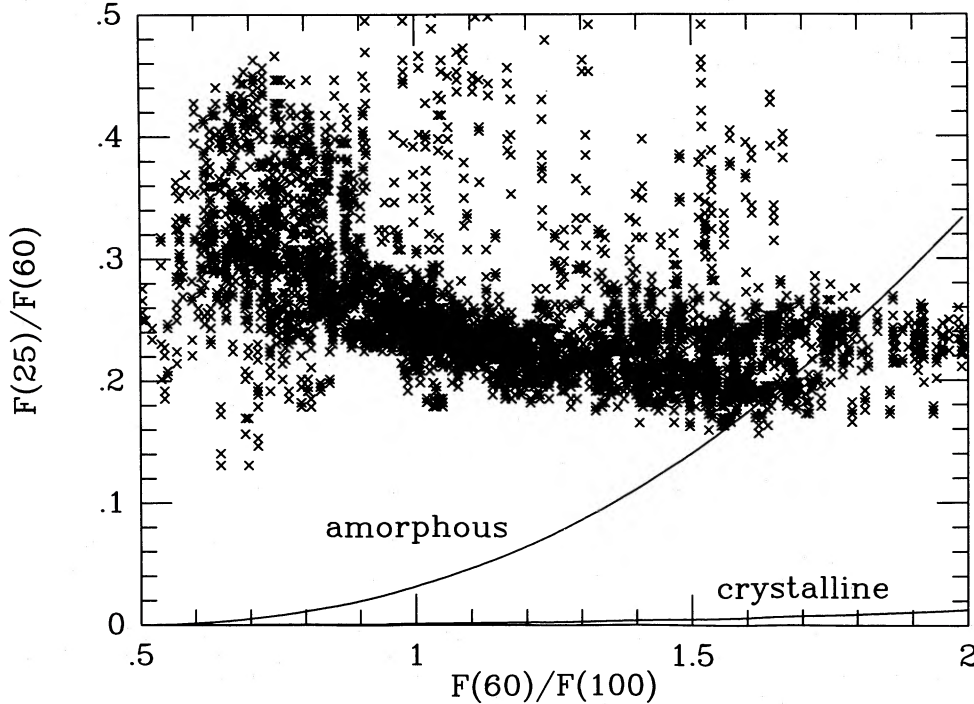


FIG. 6.—Plot of *IRAS* 25 to 60 μm vs. 60 to 100 μm in-band flux ratios. Ophiuchus cloud data points (*crosses*) do not follow the theoretical behavior of either the amorphous or crystalline model curves in thermal equilibrium. Data points are taken from the high ambient radiation field area between region B (Fig. 2) and HD 147889.

absorption efficiency of the i grain component, and $\int d\Omega = \pi r_*^2/d^2$, where d is the distance to each star in the plane of the sky and r_* is stellar radius. The $t(\lambda)$, $t'(\lambda)$, and $t''(\lambda)$ are transmission factors of intervening dust calculated from the mean interstellar extinction curve. The flux incident from the Sco OB2 association, $\int_\lambda F_{\lambda\text{Sco}} d\lambda$, was set to 6.3×10^{-2} ergs $\text{s}^{-1} \text{cm}^{-2}$ (Ryter *et al.*). Each grain component of the amorphous and crystalline models is assumed to be in thermal equilibrium having a temperature T_i defined by

$$F_i = 4\pi \int_{10 \mu\text{m}}^{750 \mu\text{m}} B_\lambda(T_i) Q_i(\lambda) d\lambda, \quad (6)$$

since a grain's emitted flux equals its absorbed flux under the condition of thermal equilibrium. The temperatures of each component of the amorphous and crystalline models were calculated at locations A and B in Figure 2 from equations (5) and (6). The flux contribution of each component at temperature T_i was weighted by its relative abundance A_i and integrated over the *IRAS* 60 and 100 μm bandpasses to produce ratio

$$\frac{\sum A_i \int_{\lambda 60} B_\lambda(T_i) Q_i(\lambda) R(\lambda) d\lambda}{\sum A_i \int_{\lambda 100} B_\lambda(T_i) Q_i(\lambda) R(\lambda) d\lambda}. \quad (7)$$

Both models have only two components (carbon and silicate) in the sums in equation (7) and the $R(\lambda)$ are *IRAS* system response factors. Equations (5), (6), and (7) were sequentially evaluated for different mean cloud densities which directly affect the transmission factors $t(\lambda)$, $t'(\lambda)$, and $t''(\lambda)$ in equation (5) until equation (7) matched the observed 60 to 100 μm *IRAS* band flux ratios at locations A and B in Figure 2 (0.46 and 1.0, respectively). The crystalline model meets this criteria for a uniform cloud density of molecular hydrogen $n(\text{H}_2) = 1400 \text{ cm}^{-3}$. The amorphous model produces a predicted flux ratio

(Eq. [7]) of only 0.75 at location B even for no interstellar absorption [$n(\text{H}_2) = 0$]. This dictates that the luminosity incident on the cloud is at least a factor of 1.7 greater than that produced by known sources if amorphous grains are responsible for emission in the *IRAS* 60 and 100 μm bands. This is in direct conflict with our result of the cloud's energy balance analysis; we concluded that all of the cloud's luminosity could be explained in terms of known sources. We therefore claim that the cloud's grains are better represented by the crystalline model than by the amorphous model and the mean density of the cloud is $n(\text{H}_2) = 1400$ from this radiative analysis. Amorphous grains are ruled out even if there is no absorbing material between the dominant luminosity sources (i.e., HD 147889) and the bulk of the cloud as might be the case if HD 147889 were exterior to the cloud and irradiating its front surface.

The optical depths at 60 μm were converted to total hydrogen column densities via competing grain models and compared to hydrogen column densities from optically thin C^{18}O for areas A and B in the cloud core. We interpret the ratios of these gas column densities as the fraction of distance into the cloud that the grains are heated. This column density ratio is a measure of surface heating because the exciting illumination appears to predominantly strike the front of the cloud; the cloud's deeply embedded infrared sources are not its most luminous ones (Fig. 1). The dominant luminosity source HD 147889 is obscured by only $A_v = 4.3$ mag (Chini 1981), while the cloud is up to $A_v = 100$ mag deep in the core region (WL, Lada and Wilking 1984). The 12 μm map (Fig. 3), a tracer of direct ultraviolet excitation, shows an abrupt factor of 2 change in flux at the western edge of the cloud core. This suggests that the core region is located behind HD 147889 and is being shadowed by a reef of material just to the east of HD

147889 and is being shadowed by a reef of material just to the east of HD 147889.

We now convert the computed 60 μm band optical depths (eq. [2]) to equivalent inferred hydrogen column densities N_{H} via three grain models. The first grain model is the MRN/DL crystalline model studied in our radiative analysis. Its grain emissivities are approximated by an $\epsilon \propto \lambda^{-2}$ emissivity law to better than 2% over the IRAS 60 and 100 μm bandpasses. We also evaluate the total hydrogen column densities predicted by the amorphous Rowan-Robinson (1986) model previously outlined and Hildebrand's (1983) amorphous model. Both of these models are well represented by an $\epsilon \propto \lambda^{-1}$ emissivity law in the IRAS 60 and 100 μm bands. We therefore used the optical depth map produced by the λ^{-2} emissivity law in determining N_{H} from the DL model and used the $\epsilon \propto \lambda^{-1}$ map in evaluating N_{H} with Rowan-Robinson and Hildebrand (1983) models. We include the $\epsilon \propto \lambda^{-1}$ models for interest and completeness even though we have shown that their grains are incapable of being heated to observed temperatures in the cloud's radiation field. Finally we compare each model's predicted N_{H} to total hydrogen column densities N_{Htot} derived from C^{18}O data.

The MRN/DL model calls for graphite and crystalline silicate grains with the previously described size distribution function (eq. [4]). This model features a grain size range from 5 nm up to 0.25 μm and we also examine Désert's (1986) modification of this model's minimum grain size to 10 nm. Rowan-Robinson (1986) prescribes several small sizes (10 nm and 30 nm) of graphite and silicate grains with DL emissivities which supplement large 0.1 μm amorphous carbon and silicate grains with λ^{-1} emissivities over the 60 and 100 μm IRAS bands. Hildebrand's model (1983) is more empirical; he specifies a $\epsilon \propto \lambda^{-1}$ emissivity with a mean grain size of 0.1 μm .

Integrations over the particle sizes, emissivities, and the IRAS 60 μm bandpass produced a value of N_{H}/τ_{60} for each model:

$$\frac{N_{\text{H}}}{\tau_{60}} = \frac{\sum_{i=1}^n H/A_i N_i}{n \sum_{i=1}^n N_i \langle \sigma_i Q_i \rangle} \quad (8)$$

for n grain species with abundances A_i/H , where

$$\langle \sigma_i Q_i \rangle = \frac{\int_{a_i} \int_{\lambda 60} \pi a_i^2 Q_i t_{\lambda} d\lambda dn(a_i)}{\int_{a_i} \int_{\lambda 60} t_{\lambda} d\lambda dn(a_i)} \quad (9)$$

The values of N_{H}/τ_{60} for each model are presented in Table 2. Next we compute total hydrogen column densities from

$$N_{\text{Htot}} = N_{\text{C}^{18}\text{O}} \times 5.0 \times 10^6 \quad (10)$$

(WL) for regions A and B. These column densities were divided into the total hydrogen column densities computed from the dust models and the resulting values are dust-heating depths for each model. We present these depths and N_{H} values calcu-

TABLE 2
MODEL GAS-TO-DUST RATIOS

GRAIN MODEL	N_{H}/τ_{60}
MRN/DL	2.78×10^{23}
MRN/DL/Désert	2.98×10^{23}
R-R	1.75×10^{23}
Hildebrand	1.30×10^{24}

TABLE 3

ρ OPH HEATING DEPTHS

REGION	MRN/DL		ROWAN-ROBINSON		HILDEBRAND	
	N_{H}	Depth	N_{H}	Depth	N_{H}	Depth
A.....	3.7×10^{21}	0.074	6.5×10^{20}	0.013	4.2×10^{21}	0.083
B.....	1.3×10^{22}	0.20	1.2×10^{21}	0.018	7.6×10^{21}	0.12

lated from Table 2 and equation (2) in Table 3 for regions A and B.

The 60 and 100 μm band grain emissions observed near HD 147889 (i.e., regions A and B) must arise from the star's photons heating grains in the cloud which reradiate in these IRAS bands. This emission is characterized by a grain temperature, optical depth, and equivalent hydrogen column density for each dust model. This N_{H} only traces the depth of the dust emission while a N_{Htot} computed from $N_{\text{C}^{18}\text{O}}$ is the true value for the cloud since the tracer molecule is optically thin. The ratio of these N_{H} values represents a dust heating depth if the cloud is uniformly heated to the calculated grain temperature or lower deeper into the cloud. Radiative transfer in an absorptive medium dictates that this is not actually the case; there must be a range of temperatures in a column and the calculated grain temperature is only a fit to that range. Nevertheless, the ratio of hydrogen column densities is interpreted as a heating depth for the purposes of evaluating the studied dust models. The general spatial agreement between dust optical depth and $N_{\text{C}^{18}\text{O}}$ in Figure 2 indicates that the dust emission is a tracer of the cloud's gross features. This good agreement suggests that the infrared emission must originate from a substantial depth in the cloud since the observed C^{18}O emission originates throughout the cloud which is known to have a complex internal density structure (Loren *et al.* 1980).

Table 3 presents the heating depths of regions A and B for the three models studied. The MRN/DL model N_{H} and heating depth values increase slightly (7%) if it is modified for larger a_{min} as suggested by the color-color fits to Désert's model. The illumination geometry suggest that both regions A and B have heating depths of a few percent or more because they are near the embedded source HD 147889.

The MRN/DL and Hildebrand models' depths are consistent with this, but it appears that the Rowan-Robinson depths are inconsistent with this requirement. All models give higher depths for region B which is closer to HD 147889. The Ophiuchus dust appears to be well described by the MRN/DL crystalline grain model as revealed in our radiative modeling of grain temperatures so we assert that the MRN/DL model correctly calculates heating depths. However, great uncertainties are involved in the calculation of N_{H} from dust models; our adopted conversion factor of $N_{\text{C}^{18}\text{O}}$ to N_{Htot} in equation (10) is a factor of 2 greater than another value computed for the same molecular cloud (Frerking, Langer, and Wilson 1982). The computed heating depths are therefore highly uncertain; the Frerking *et al.* C^{18}O conversion factor would lower these values by 50% in Table 3. We suggest that our computed heating depths are reasonable upper limits.

IV. SUMMARY

This analysis of the equilibrium process dust emission in the ρ Oph cloud has yielded the following results.

1. The luminosity of the cloud closely matches the lumin-

osity of the cloud's known embedded and external radiation sources. There is no evidence for a large population of undetected low-luminosity sources within the cloud and unknown external heating is also only a minor source of energy. Most of the cloud's luminosity is emitted in the mid-to-far-infrared (40 to 250 μm). A grain emissivity law cannot be chosen from an energy balance requirement; the differences in cloud luminosities predicted by both laws is on the order of the uncertainties in the calculations of flux absorbed by the Sco OB2 association and in the cloud's unobserved scattered ultraviolet and visible radiation.

2. Dust temperature maps indicate that the dust is not hot enough to heat the gas to observed temperatures. A simple cloud model with a radiation field composed of flux HD 147889, S1, and the Sco OB2 association predicts the observed IRAS 60 to 100 μm in-band flux ratios for a mean cloud density $n(\text{H}_2) = 1400$, provided a MRN/DL crystalline grain model is adopted. The model demonstrates that known radiation sources are not strong enough to heat amorphous grains ($\epsilon \propto \lambda^{-1}$) to the temperatures required by the IRAS data. The cloud's observed luminosity precludes the existence of substantial additional radiation sources.

3. Flattened 12 and 25 μm IRAS SURVEY CO-ADD frames show much extended emission in these bands, suggesting stochastic heating of very small grains or large molecules. The 25 μm band is dominated by nonthermal emission even in areas of high ambient radiation field values (Fig. 6). Désert's grain model (1986) and our color-color plots (Figs. 4 and 5) indicate a larger than normal minimum value of grain size in the MRN grain distribution, and they also confirm a population of very small grains or PAH molecules. These results are

in agreement with previous studies of the ρ Ophiuchi region (Young, Lada, and Wilking 1986; Vrba *et al.* 1975), but now the minimum equilibrium particle size in an MRN distribution is found to be 10 nm. Figure 4 also suggests that regions with many embedded young stellar objects have lower $F_{\nu}(12)/F_{\nu}(25)$ than more barren areas, suggesting that PAH molecules are dissociated in the radiation field surrounding these objects.

4. The 60 μm band dust optical depth map is generally similar to the optically thin $N_{\text{C}180}$ map in the cloud core. Differences in the maps are interpreted as differences in the depths to which the dust is heated since a constant gas-to-dust ratio is assumed over the core region. Artificially low dust optical depth values also arise at the locations of embedded infrared sources.

5. Column densities of hydrogen have been computed from the 60 μm dust optical depth map for three major grain material and size distribution models. The Hildebrand model and MRN/DL/Désert models give dust heating depths which are consistent with cloud geometry. We suggest that the MRN/DL/Désert model heating depths are correct since only its crystalline grains can be heated to the observed dust temperatures in the cloud's radiation field. The good correlation between τ_{60} and $N_{\text{C}180}$ maps (Fig. 2) also suggests that a considerable fraction of the cloud's interior is heated as predicted by the MRN/DL/Désert model. Grains are therefore heated to approximately 10% to 20% of the cloud's depth in the core region.

This work was supported in part by the IRAS Data Analysis program under JPL contract 957396.

REFERENCES

- Bohlin, R. C., and Savage, B. D. 1981, *Ap. J.*, **249**, 109.
 Carrasco, L., Strom, S. E., and Strom, K. M. 1973, *Ap. J.*, **182**, 95.
 Chini, R. 1981, *Astr. Ap.*, **99**, 346.
 Désert, F. X. 1986, in *Light on Dark Matter*, ed. F. P. Israel (Dordrecht: Reidel), p. 213.
 Draine, B. T., and Lee, H. M. 1984, *Ap. J.*, **285**, 89 (DL).
 Draine, B. T., and Anderson 1985, *Ap. J.*, **292**, 494.
 Elias, J. H. 1978, *Ap. J.*, **224**, 453.
 Encrenaz, P. J., Falgarone, E., and Lucas, R. 1975, *Astr. Ap.*, **44**, 73.
 Freking, M. A., Langer, W. D., and Wilson, R. W. 1982, *Ap. J.*, **262**, 590.
 Grasdalen, G. L., Storm, K. M., and Strom, S. E. 1973, *Ap. J. (Letters)*, **184**, L53.
 Harris, D. H., Woolf, N. J., and Rieke, G. H. 1978, *Ap. J.*, **226**, 829.
 Hildebrand, R. H. 1983, *Quart. J.R.A.S.*, **24**, 267.
 IRAS Explanatory Supplement, 1984, ed. C. A. Beichman, G. Neugebauer, H. J. Habing, P. E. Clegg, and T. J. Chester (JPL Pub.D-1855).
 Lada, C. J., and Wilking, B. A. 1980, *Ap. J.*, **238**, 620.
 ———. 1984, *Ap. J.*, **287**, 610.
 Léger, A., and Puget, J. L. 1984, *Astr. Ap.*, **137**, L5.
 Lonsdale, C. J., Helou, G., Good, J. C., and Rice, W. 1985, *Catalogued Galaxies and Quasars in the IRAS Survey* (Pasadena: NASA Jet Propulsion Laboratory).
 Loren, R. B., Wotten, A., Sandqvist, AA., and Bernes, C. 1980, *Ap. J. (Letters)*, **240**, L165.
 Mathis, J. S., Rumpl, W., and Nordsieck, K. H. 1977, *Ap. J.*, **217**, 425 (MRN).
 McMillan, R. S. 1978, *Ap. J.*, **225**, 417.
 Purcell, E. M. 1969, *Ap. J.*, **158**, 433.
 Rengarajan, T. N. 1984, *Astr. Ap.*, **140**, 213.
 Rowan-Robinson, M. 1986, *M.N.R.A.S.*, **219**, 737.
 Rytter, C., Puget, J. L., and Perault, M. 1988, *Astr. Ap.*, in press.
 Sellgren, K. 1984, *Ap. J.*, **277**, 623.
 Smithsonian Astrophysical Observatory. 1986, *Star Catalog* (Washington, DC: Smithsonian Institution) (SAO).
 van Breda, I. G., Glass, I. S., and Whittet, D. C. B. 1974, *M.N.R.A.S.*, **168**, 551.
 Vrba, F. J., Strom, K. M., Strom, S. E., and Grasdalen, G. L. 1975, *Ap. J.*, **197**, 77.
 Whittet, D. C. B. 1974, *M.N.R.A.S.*, **168**, 371.
 Wilking, B. A. 1981, Ph.D. thesis, University of Arizona.
 Wilking, B. A., and Lada, C. J. 1983, *Ap. J.*, **274**, 698 (WL).
 Young, E. T., Lada, C. J., and Wilking, B. A. 1986, *Ap. J. (Letters)*, **304**, L45.

T. P. GREENE and E. T. YOUNG: Steward Observatory, University of Arizona, Tucson, AZ 85721